PHYSICAL SCIENCE

Efficient oxygen reduction catalysis by subnanometer Pt alloy nanowires

Kezhu Jiang,[1] Dandan Zhao,[1] Shaojun Guo,[2,3,4]* Xu Zhang,[5] Xing Zhu,[6] Jun Guo,[6] Gang Lu,[5] Xiaoqing Huang[1]*

The common knowledge is that Pt and Pt alloy nanoparticles (NPs) less than 2 nm are not desirable for oxygen reduction reaction (ORR). However, whether the same trend is expected in Pt-based nanowires (NWs) and nanoplates remains questionable because there is no scalable approach to make such Pt nanostructures. We report a general approach for preparing subnanometer Pt alloy NWs with a diameter of only 4 to 5 atomic layer thickness, ranging from monometallic Pt NWs to bimetallic PtNi and PtCo NWs and to trimetallic PtNiCo NWs. In a sharp contrast to Pt alloy NPs, the subnanometer Pt alloy NWs demonstrate exceptional mass and specific activities of 4.20 A/mg and 5.11 mA/cm^2 at 0.9 V versus reversible hydrogen electrode (RHE), respectively, 32.3 and 26.9 times higher than those of the commercial Pt/C. Density functional theory simulations reveal that the enhanced ORR activities are attributed to the catalytically active sites on high-density (111) facets in the subnanometer Pt alloy NWs. They are also very stable under the ORR condition with negligible activity decay over the course of 30,000 cycles. Our work presents a new approach to maximize Pt catalytic efficiency with atomic level utilization for efficient heterogeneous catalysis and beyond.

INTRODUCTION

In the search for electrocatalysts with extremely high electrocatalytic activity and stability for oxygen reduction reaction (ORR), the density functional theory (DFT) results show that the ORR activity increases in the order of high-index facet>(111)≫(100) in $HClO_4$ solution, giving the important direction in obtaining practical high-performance ORR catalysts (*1*, *2*). Noble metal–based nanowires (NWs) with dominant (111) facets are, thus, of great interest as a new class of stable catalysts for boosting ORR (*3*–*7*). Although introducing high-index facets into Pt alloy NWs can enhance their intrinsic activity, those alloy NWs with large diameters still have relatively low Pt utilization. Small-size Pt alloy NWs with high-index facets can provide high ORR mass activity, but a formidable challenge is that the high-index facets in these NWs could gradually vanish under detrimental corrosive ORR conditions, resulting in the performance losses under the long-term stability test (*8*). Because the (111) facet activity is also very active and stable for ORR, decreasing the diameter of NWs to fewer atomic layers presents a more interesting system for studies because exposing surface atoms to the largest extent, increasing lattice contraction of surface atoms, and enhancing strong quantum confinement may provide a better opportunity for boosting the multiple applications in catalysis, energy storage and conversion, and electronic and sensing devices (*1*, *2*, *9*–*17*). However, for the catalysis studies, when the size of the Pt- or PtM (M, transition metal)–based nanoparticles (NPs) was reduced to less than 2 nm, they were not very active for ORR because of their strong oxygen adsorption energy (E_O) of oxygen species to Pt surface (*18*–*23*). Little knowledge is put into understanding whether the NWs with thin atomic layers can provide the enhanced catalysis, because the ability to control the synthesis of subnanometer metallic NWs with atomic layers is a great challenge (*24*, *25*). This is mainly caused by metal atoms that have a strong preference for connecting in three dimensions and their isotropic growth manner during the synthetic process (*26*–*31*).

To solve this problem, we report a robust and general strategy for the preparation of subnanometer monometallic, bimetallic, and multimetallic Pt and Pt alloy NWs with few atomic layer thickness. We found that the existence of nickel(II) acetylacetonate [$Ni(acac)_2$] plays an important role in forming Pt NWs with their length controlled by the additional molybdenum carbonyl [$Mo(CO)_6$], whereas the addition of reducing agent (glucose) can lead to subnanometer PtNi alloy NWs. The present synthetic strategy is a general method for making different types of subnanometer bimetallic and trimetallic NWs with different compositions, depending on the transition metals used. The subnanometer Pt alloy NWs exhibit excellent electrocatalytic activity and superior stability toward ORR. The PtNiCo NWs show the highest mass activity of 4.20 A/mg and specific activity of 5.11 mA/cm^2, which are superior to the PtNi NWs (2.97 A/mg and 3.68 mA/cm^2), Pt NWs (1.06 A/mg and 1.39 mA/cm^2), as well as the commercial Pt/C (0.13 A/mg and 0.19 mA/cm^2). DFT simulations reveal that the catalytically active sites on (111) facets of subnanometer Pt-based NWs can lead to the optimized E_O, promoting the ORR activity enhancement. The PtNi NWs show the best stability with negligible activity decay after 30,000 cycles. The newly generated subnanometer Pt alloy NWs enabled by our large scalable wet-chemical method reported here are promising catalyst candidates with greatly improved Pt utilization yet promising performance for practical proton exchange membrane fuel cells and beyond.

RESULTS AND DISCUSSION

In a typical preparation of Pt NWs, platinum(II) acetylacetonate [$Pt(acac)_2$], $Ni(acac)_2$, cetyltrimethylammonium chloride (CTAC), and $Mo(CO)_6$ were dissolved in oleylamine (OA) by sonication for 1 hour. The resulting homogeneous mixture was heated at 160°C for 2 hours in an

---

[1] College of Chemistry, Chemical Engineering and Materials Science, Soochow University, Jiangsu 215123, China. [2] Department of Materials Science and Engineering, College of Engineering, Peking University, Beijing 100871, China. [3] Beijing Innovation Center for Engineering Science and Advanced Technology, College of Engineering, Peking University, Beijing 100871, China. [4] Key Laboratory of Theory and Technology of Advanced Batteries Materials, College of Engineering, Peking University, Beijing 100871, China. [5] Department of Physics and Astronomy, California State University, Northridge, Northridge, CA 91330, USA. [6] Testing and Analysis Center, Soochow University, Jiangsu 215123, China.
*Corresponding author. Email: guosj@pku.edu.cn (S.G.); hxq006@suda.edu.cn (X.H.)

oil bath. The obtained colloidal products were collected by centrifugation and washed three times with a cyclohexane/ethanol (1:9, v/v) mixture. The preparation of PtNi NWs was similar to that of Pt NWs except for the use of glucose as a reducing agent. The synthesis of PtCo or PtNiCo NWs was similar to that of PtNi NWs, except that Ni(acac)$_2$ was replaced with cobalt(III) acetylacetonate [Co(acac)$_3$] or the combination of Ni(acac)$_2$ and Co(acac)$_3$, respectively.

The morphology and structure of the as-prepared subnanometer Pt NWs were characterized by transmission electron microscopy (TEM), high-resolution TEM (HRTEM), and high-angle annular dark-field scanning TEM (HAADF-STEM). The representative low-magnification HAADF-STEM and TEM images reveal that the NWs were the dominant products, approaching 100% yield (Fig. 1A and fig. S1). They have a highly uniform diameter of 0.8 nm, approximately 4 to 5 atomic layer thick, and with aspect ratio of ~22.5, as determined by manually measuring around 200 randomly selected NWs (Fig. 1A, right inset). The subnanometer character of Pt NWs is further visualized by high-magnification TEM and STEM (Fig. 1B and fig. S1). Energy-dispersive x-ray spectroscopy (EDS; Fig. 1C) and x-ray photoelectron spectroscopy (XPS; fig. S2) of Pt NWs reveal that they are composed of only Pt without any Ni or Mo. The selected area electron diffraction (SAED) (Fig. 1A, left inset) and powder x-ray diffraction (PXRD) patterns (Fig. 1D) show that they have the representative face-centered cubic (fcc) structure. The relative intensity of the (111) plane is much higher than that of the standard fcc Pt [Joint Committee on Powder Diffraction Standards (JCPDS) no. 04-0802], indicating that the subnanometer Pt NWs have rich (111) facets (*32*). The subnanometer Pt NWs were further investigated by HRTEM to evaluate their structural characteristics (Fig. 1E and fig. S3). They are single crystalline with a spacing distance of 0.228 nm, being consistent with the (111) lattice plane of fcc Pt.

Note that the addition of Ni(acac)$_2$ in the synthetic system could only lead to Pt NWs instead of PtNi NWs because of the limited reducing ability of OA. In this regard, we tried to use a stronger reducing agent (glucose) to make Pt alloy NWs. The use of additional glucose could make long and subnanometer PtNi NWs. The low-magnification HAADF-STEM and TEM images reveal that the abundant NWs were the dominant products (Fig. 2A and fig. S4). The PtNi NWs here exhibit high aspect ratios of ~150 with average length of 120 nm and uniform diameter as thin as 0.8 nm, approximately 4 to 5 atomic layer thick (Fig. 2A, right inset). The high-magnification HAADF-STEM and TEM images show that an individual NW has a smooth surface along its whole length with subnanometer feature (Fig. 2, B and C). The HRTEM image reveals that the subnanometer PtNi NWs have the lattice spacings of 0.223 nm, slightly smaller than that of the (111) lattice plane of Pt (0.228 nm; Fig. 2E and fig. S5), implying that the PtNi NWs are also enclosed by (111) facets. The TEM-EDS pattern of PtNi NWs reveals that they are composed of Pt and Ni with the Pt/Ni composition at 74.8/25.2 (Fig. 2F), which is in accordance with the inductively coupled plasma atomic emission spectroscopy (ICP-AES) result. The SAED (Fig. 2A, left inset) and PXRD patterns (Fig. 2G) of PtNi NWs also show an fcc structure, with diffraction peak positions shifted to high value, further revealing the formation of the alloy structure. The relative intensity of the (111) plane of PtNi NWs is higher than that of the standard fcc Pt, giving important information about the PtNi NWs with (111)-dominated surfaces (*32*). The broadened diffraction peaks imply their

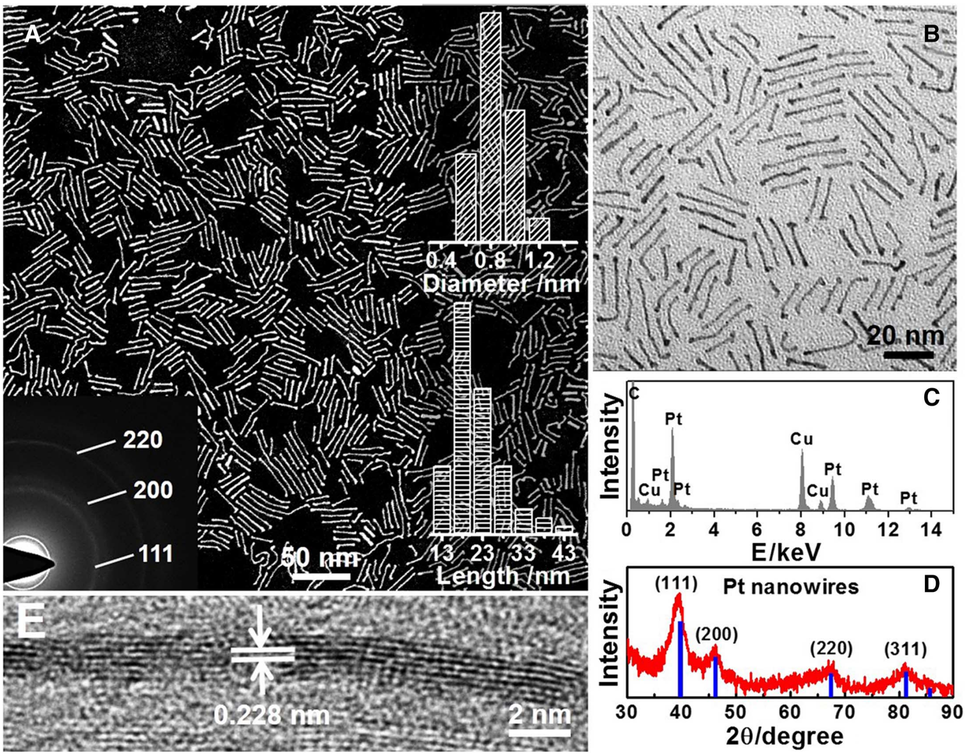

Fig. 1. Morphology and structure characterizations of subnanometer Pt NWs. Representative (**A**) STEM image, (**B**) TEM image, (**C**) TEM-EDS spectrum, (**D**) PXRD pattern, and (**E**) HRTEM image of subnanometer Pt NWs. The standard diffraction (Pt, JCPDS no. 04-0802) is drawn using blue lines in (D). The left inset of (A) shows the SAED of subnanometer Pt NWs. The right inset of (A) shows the histograms of diameter and length of subnanometer Pt NWs.

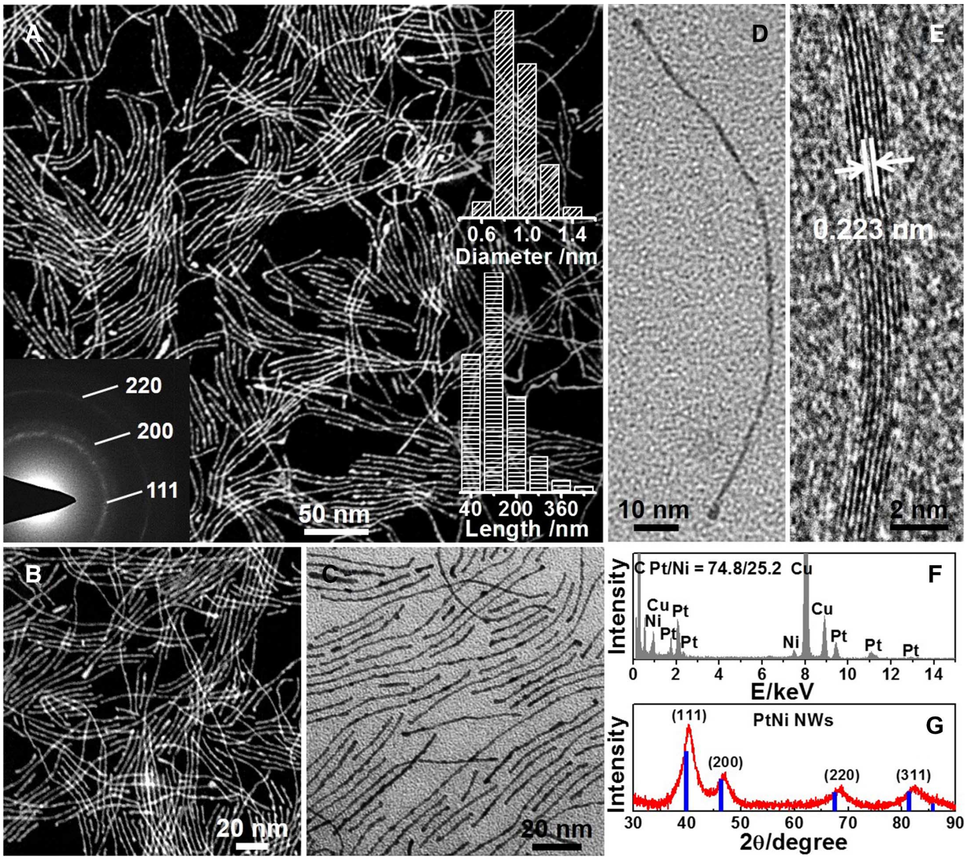

Fig. 2. Morphology and structure characterizations of subnanometer PtNi NWs. Representative (**A** and **B**) STEM and (**C**) TEM images of subnanometer PtNi NWs. (**D**) TEM and (**E**) HRTEM images of two PtNi NWs. (**F**) TEM-EDS spectrum and (**G**) PXRD pattern of subnanometer PtNi NWs. The standard diffraction (Pt, JCPDS no. 04-0802) is drawn using blue lines in (G). Left inset of (A) shows SAED pattern of subnanometer PtNi NWs. Right inset of (A) shows the histograms on the diameter and length of subnanometer PtNi NWs.

suprathin feature. The subnanometer PtNi NWs were further characterized by the EDS line scan, which helped in the understanding of the distribution of Pt and Ni, showing that the Ni concentrates on the core region and Pt distributes evenly across the whole NW. This indicates the formation of Pt-rich shell on the NWs (fig. S6), which is in accordance with the composition results on the PtNi NW surface and bulk analyzed by ICP, EDS, and XPS (table S1).

The important feature of the present synthetic method is that it is a general method for making different types of subnanometer bimetallic and trimetallic NWs, such as PtCo and PtNiCo. The PtCo NWs have an average diameter of 0.8 nm and lengths of several decade nanometers (Fig. 3A and fig. S7, A and B). The HRTEM image of PtCo NWs shows the lattice distance of 0.224 nm, attributed to the (111) plane of the Pt alloy (Fig. 3B). The fcc crystal phase was confirmed by the PXRD, and the composition of PtCo was determined by scanning electron microscopy (SEM)–EDS (fig. S7, E and F). By replacing Ni(acac)$_2$ with the combination of Ni(acac)$_2$ and Co(acac)$_3$, the PtNiCo NWs with the similar diameter could also be produced (Fig. 3C). The morphology and structure of subnanometer PtNiCo NWs were further characterized by TEM, HRTEM, PXRD, EDS, and EDS line scan (Fig. 3D and figs. S8 and S9). Besides controlling Pt-based NWs at compositions, the length of subnanometer Pt-based NWs could be easily controlled by changing the amounts of Mo(CO)$_6$ with the other synthesis parameters unchanged. When 2 mg of Mo(CO)$_6$ was used, the average lengths of NWs could reach up to ~9 nm (fig. S10, A and B). By increasing the amount of Mo(CO)$_6$ to 3 mg, the average length of NWs was about 18 nm. Increasing the amount of Mo(CO)$_6$ to 4 mg led to the NWs having an average length of ~35 nm (fig. S10, E and F). The SEM-EDS patterns show that the abovementioned NWs with a different length only exhibit Pt signal (fig. S10I), whereas their PXRD patterns demonstrate the typical fcc Pt diffraction peaks (fig. S10J), revealing that these NWs are composed of Pt.

To better understand the growth mechanism of the Pt NWs, we investigated the intermediates collected at different reaction times by TEM (fig. S11). The product collected after a 10-min reaction time was dominated by many small NPs and partial short NWs (fig. S11A). With the increase in reaction time, the coalescence of NPs occurred to form NWs and eventually longer NWs with a diameter of only ~0.5 nm (fig. S11B). After a 30-min reaction time, the Pt NWs were formed and grew in length and diameter (fig. S11C). The Pt NWs with lower aspect ratios were produced after reacting for 90 min, and no further obvious change was observed when the reaction time was prolonged to 120 min (fig. S11, D to F). The abovementioned experimental results show that Pt NWs were made from the small NPs, and the growth of the Pt NWs was controlled by the oriented attachment mechanism and Ostwald ripening process (*27*, *28*). To further achieve fine control over the Pt NWs, we thoroughly investigated the effect of different experimental parameters on the morphologies of

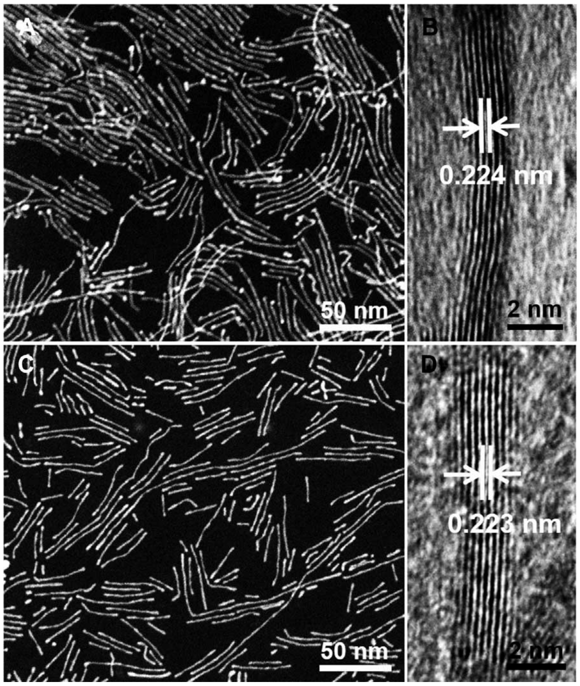

Fig. 3. Morphology and structure characterizations of subnanometer PtCo and PtNiCo NWs. Representative STEM (**A** and **C**) and HRTEM (**B** and **D**) images of subnanometer (A and B) PtCo and (C and D) PtNiCo NWs.

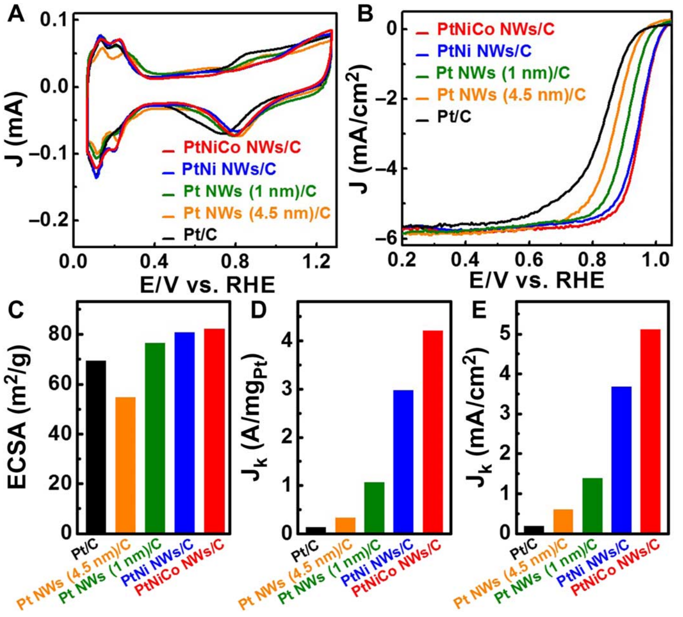

Fig. 4. Electrocatalytic performance of PtNiCo NWs/C, PtNi NWs/C, Pt NWs (1 nm)/C, Pt NWs (4.5 nm)/C, and commercial Pt/C. (**A**) CVs recorded at room temperature in 0.1 M $HClO_4$ solution at a sweep rate of 50 mV/s. (**B**) ORR polarization curves recorded at room temperature in an O_2-saturated 0.1 M $HClO_4$ aqueous solution at a sweep rate of 10 mV/s and a rotation rate of 1600 rpm. (**C**) ECSAs, (**D**) mass activities, and (**E**) specific activities of PtNiCo NWs/C, PtNi NWs/C, Pt NWs (1 nm)/C, Pt NWs (4.5 nm)/C, and commercial Pt/C.

resulting NWs. The absence of $Mo(CO)_6$ in the synthetic method could just yield the heavily aggregated NPs (fig. S12, A and B). To further explore whether Mo or the carbonyl group in $Mo(CO)_6$ was necessary in our synthesis, $Mo(CO)_6$ was replaced by tungsten carbonyl [$W(CO)_6$]. The NWs could still be made (fig. S12, C and D), suggesting that carbonyl was the structure-directing agent for the formation of subnanometer Pt NWs likely due to the strong adsorption of carbonyl on Pt atoms (*3*, *33*). As evidenced by TEM images, without the introduction of $Ni(acac)_2$, small particles mixed with NWs were the dominant product (fig. S13, A and B). When $Ni(acac)_2$ was replaced by the same amount of nickel(II) chloride ($NiCl_2$) or nickel(II) acetate [$Ni(Ac)_2$], similar subnanometer Pt NWs were formed (fig. S13, C to F). If we changed $Ni(acac)_2$ to iron(III) acetylacetonate [$Fe(acac)_2$], the NWs could also be obtained, indicating that transition metal cations play an important role in mediating the formation of Pt NWs (fig. S14) (*28*, *33*–*35*). Another interesting point is that in the present synthetic method, the morphology of the product was also affected by the surfactant (CTAC). The reaction in the absence of CTAC could yield just the small NPs with the size of 5.2 ± 1 nm (fig. S15, A and B). The product with a low percentage of NWs was obtained by changing the amount of CTAC from 32 to 16 or 64 mg (fig. S15, C to F). Thus, the use of a proper amount of CTAC was also crucial to form subnanometer Pt NWs (*36*). Here, the carbonyl, Ni^{2+}, and CTAC played important roles in the formation of subnanometer Pt NWs, and the amount of carbonyl was useful to control the length of Pt NWs.

The subnanometer Pt, PtNi, and PtNiCo NWs were studied as catalysts for electrochemical reduction of oxygen. Before the ORR measurements, they were first deposited on carbon support via the sonication of the mixture of NWs and carbon in cyclohexane/ethanol (1:1, v/v) and then washed three times with the mixture of cyclohexane and ethanol. These treatments allow the subnanometer NWs to be uniformly distributed on carbon and to also remove the organic species from NWs (fig. S16). The final products were denoted as Pt NWs (1 nm)/C, PtNi NWs/C, and PtNiCo NWs/C, respectively (fig. S17 to S19). Then, the catalysts were suspended in a mixture of isopropanol/water/Nafion (89:10:1, v/v/v) with a concentration of 0.25 mg_{Pt}/ml. A 5-μl aliquot of the suspension was deposited onto a glassy carbon electrode and dried under ambient condition. The ~4.5-nm Pt NWs were also prepared as a comparison (fig. S20) (*37*). The loading amounts of Pt were measured to 1.25 μg for Pt NWs (1 nm)/C, Pt NWs (4.5 nm)/C, PtNi NWs/C, PtNiCo NWs/C, and Pt/C catalysts. The cyclic voltammograms (CVs) of these catalysts were recorded in an N_2-purged 0.1 M $HClO_4$ solution at a sweep rate of 50 mV/s (Fig. 4A). Figure 4B shows the ORR polarization curves of different catalysts recorded at room temperature at a sweep rate of 10 mV/s and a rotation rate of 1600 rpm in O_2-saturated 0.1 M $HClO_4$. The underpotentially deposited hydrogen adsorption charge is used to estimate the electrochemical surface area (ECSA) of the abovementioned catalysts. The PtNiCo NWs/C displays an outstandingly high ECSA of 82.2 m^2/g, higher than those of PtNi NWs/C (80.7 m^2/g), Pt NWs (1 nm)/C (76.4 m^2/g), Pt NWs (4.5 nm)/C (54.6 m^2/g), and the commercial Pt/C catalyst (69.3 m^2/g) (Fig. 4C). The kinetic currents, calculated from the polarization curves at 0.9 V versus RHE by using the mass transport correction, were normalized to ECSA and Pt loading amount to obtain the specific and mass activities. The Pt NWs (1 nm)/C can deliver the ORR mass and specific activities of 1.06 A/mg and 1.39 mA/cm^2, which are much higher than those of Pt NWs (4.5 nm)/C (0.33 A/mg and 0.6 mA/cm^2), showing the advantages of subnanometer Pt NWs (1 nm). In addition, the Pt NWs (1 nm) with different lengths show similar ORR activities (fig. S21), suggesting that the length of the NWs may be not the main factor for high ORR activity, whereas the exposed (111) facet is the key for high ORR activity. The mass activity of PtNiCo NWs/C reaches 4.20 A/mg at 0.9 V versus RHE, 1.4-, 4.0-, 12.7-, and 32.3-fold higher than those of PtNi NWs/C (2.97 A/mg), Pt NWs (1 nm)/C (1.06 A/mg), Pt NWs (4.5 nm)/C (0.33 A/mg), and Pt/C catalyst (0.13 A/mg; fig. S22) (Fig. 4D). The specific activity of the PtNiCo NWs/C catalyst is 5.11 mA/cm^2, with impressive improvement factors of 1.4 over PtNi NWs/C, 3.7 over Pt NWs (1 nm)/C, 8.5 over Pt NWs (4.5 nm)/C, and 26.9 over Pt/C catalyst (Fig. 4E). The mass and specific activities of the subnanometer PtNiCo NWs are much higher than other Pt-based thin NW catalysts (table S2). Such higher mass and specific activities of PtNiCo NWs, as compared with those of PtNiCo NPs, are attributed to the atomic thickness, (111)-dominated surface, and the Pt-rich shell structure, which are much different from the previously reported PtM NWs (*38*, *39*).

We further studied the electrochemical stability of the PtNiCo NWs/C and PtNi NWs/C catalysts by using an accelerated durability test between 0.6 and 1.1 V versus RHE in 0.1 M $HClO_4$ at a scan rate of 100 mV/s. Figure 5 (A, C, and E) shows the ORR polarization curves of the Pt/C, PtNi NWs/C, and PtNiCo NWs/C catalysts, respectively, after different long-term potential cycles. The changes in both the ECSA and mass activity of different catalysts were calculated. We found that the PtNi NWs/C and PtNiCo NWs/C show much higher stability with a small portion decrease in their initial ECSA and mass activity than those of the commercial Pt/C catalyst (Fig. 5, B, D, and F, and fig. S23). The PtNi NWs/C shows the best stability with almost no change in their initial ECSA (Fig. 5D), and their mass activities are still as high as 2.79 A/mg after 30,000 cycles. We found that the PtNiCo NWs have higher ECSA loss (27.6%) after 30,000 accelerated durability tests than the PtNi NWs (11.6%). The relatively worse stability of PtNiCo NWs is likely due to the higher transition metal content of PtNiCo NWs and higher reduction potential of Co, both of which can result in a more severe dissolution of transition metals in the PtNiCo NWs, as further confirmed by EDS data (figs. S24 and S25B) (*38*, *40*). In contrast, the Pt/C catalyst was unstable under the same reaction conditions, with only 59.6% of the initial ECSA and 38.5% of the initial mass activity maintained after 30,000 cycles (Fig. 5B). Although under the same condition, serious aggregation was observed for the Pt/C (fig. S26). Therefore, the subnanometer PtNi NWs with atomic thickness, (111)-dominated surface, and Pt-rich shell are the key for achieving high ORR durability (*27*, *41*, *42*).

To shed light on the exceptional ORR performance of the subnanometer Pt-based NWs, we performed DFT calculations for the E_O on the Pt alloy NWs. E_O has been widely used as a descriptor for ORR activities, and there exists an optimal value of E_O, for which the ORR activity reaches the maximum (*43*, *44*). For convenience, we shift the optimal E_O value to 0 eV and use ΔE_O to represent the difference of a

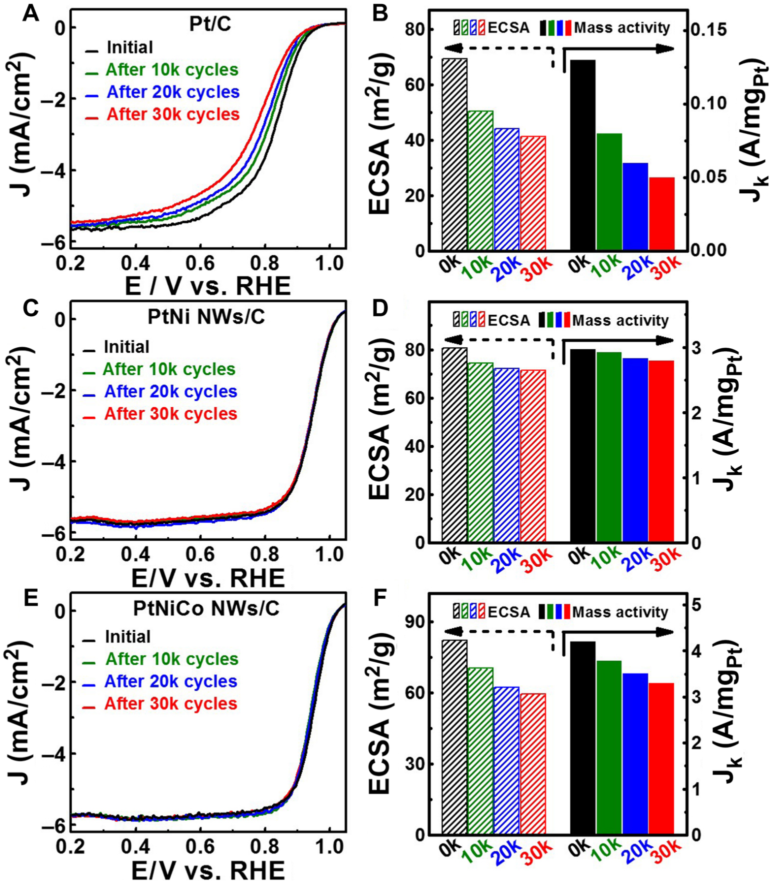

Fig. 5. Electrocatalytic durability of subnanometer PtNiCo NWs, PtNi NWs, and commercial Pt/C. ORR polarization curves of (**A**) Pt/C, (**C**) PtNi NWs, and (**E**) PtNiCo NWs before and after different potential cycles between 0.6 and 1.1 V versus RHE. The ORR polarization curves were recorded at room temperature in an O_2-saturated 0.1 M $HClO_4$ aqueous solution at a sweep rate of 10 mV/s and rotation rate of 1600 rpm. The changes in ECSA and mass activities of (**B**) Pt/C, (**D**) PtNi NWs, and (**F**) PtNiCo NWs before and after different potential cycles.

given E_O value relative to this optimal reference. In accordance with our HRTEM and HAADF-STEM measurements, we model the subnanometer NW as a single crystal terminated by four (111) and two (100) facets (Fig. 6A). The diameter of the subnanometer NW is about 0.8 nm, which is 4 to 5 atomic layer thick. Thus, the top layer of our DFT models consists of pure Pt. The four most stable oxygen adsorption sites on each facet and edge of the NWs are examined (Fig. 6B): the fcc hollow sites on the (111) facet ("NW 111"), the bridge site on the (100) facet ("NW 100"), the bridge site on the edge, which is the intersection of two (111) facets ("NW edge1"), and the bridge site on the edge, which is the intersection of (111) and (100) facets ("NW edge2"). Moreover, we also calculated ΔE_O on the flat (111) surface of Pt ("flat 111"). The results of ΔE_O are shown in Fig. 6C. We found that the NW 111 site is highly active for ORR, whose ΔE_O value is much closer to zero than that on the Pt flat 111 site. This higher ΔE_O value on the NW 111 site originates from a compressive strain of 1.5% on the (111) facet of the subnanometer NW. The superior ORR activity of the subnanometer Pt NWs compared to that of the Pt NPs is probably attributed to these catalytically active sites on the (111) facets, which are rich in the subnanometer NWs. The presence of Ni could relieve the undesirable overbinding between the NW and the oxygen atoms (Fig. 6C), further enhancing the ORR activity. Moreover, for PtNi NWs, more adsorption sites become active for ORR, such as the NW 100 and NW edge1 sites whose ΔE_O values are comparable to those on the flat 111 surface. This suggests that PtNi NWs have superior ORR activity as compared with the Pt NWs, consistent with the experimental observations. Therefore, both the ligand and the strain effect are responsible for the much enhanced ORR activities on the NWs.

To summarize, we report a new solvothermal approach to make a new class of subnanometer Pt and Pt alloy NWs with atomic level size, tunable composition, and aspect ratio (figs. S27 to S30). The diameter of the NWs is as thin as 0.8 nm, only 4 to 5 atomic layer thick. The length of the NWs can be easily controlled from 9 to 35 nm by changing the amount of $Mo(CO)_6$. The key for making subnanometer Pt alloy NWs is the addition of glucose as a reducing agent. The present strategy can be generalized to make other subnanometer Pt alloy NWs (such as PtCo and PtNiCo), depending on the use of different transition metal precursors. Because of their atomic level character and alloy effect, the subnanometer PtNi and PtNiCo NWs have the obvious advantage in boosting ORR with high activity and stability. The PtNiCo NWs can deliver the ORR mass and specific activities of 4.20 A/mg and 5.11 mA/cm^2 that are 32.3 and 26.9 times higher than those of the state-of-the-art commercial Pt/C catalyst. DFT studies indicate that the exceptionally high ORR activities on the subnanometer Pt-based NWs originate from the catalytically active hollow sites on the (111) facets of atomic level NWs. The PtNi NWs also exhibit excellent electrochemical durability under the ORR condition with negligible activity decay over the course of 30,000 cycles. We believe that those newly created subnanometer Pt alloy NWs with largely improved Pt utilization yet promising ORR performance will hold great promise for sensing heterogeneous catalysis and beyond.

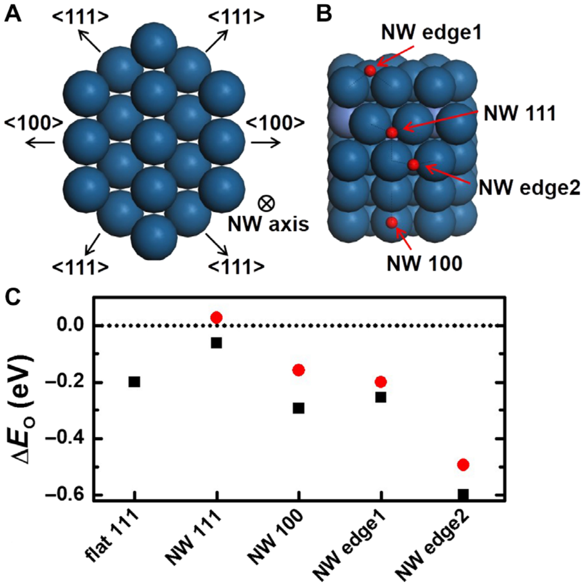

Fig. 6. DFT calculations of E_O. (**A**) Atomic model of the single crystalline NW with four (111) facets and two (100) facets. (**B**) Four stable adsorption sites for oxygen on the NW. Red spheres represent oxygen atoms. (**C**) ΔE_O on flat Pt (111) surface and Pt-based NWs. The black squares and red circles correspond to ΔE_O values on the pure Pt and PtNi NW, respectively. The horizontal dashed line indicates the optimal ΔE_O value.

MATERIALS AND METHODS

Chemicals

$Co(acac)_3$ (97%), $Pt(acac)_2$ (97%), $Ni(acac)_2$ (97%), CTAC (AR), octadecylamine (ODA, AR), and OA (68 to 70%) were all purchased from Sigma-Aldrich. Nickel(II) chloride hexahydrate ($NiCl_2{\cdot}6H_2O$, AR), nickel(II) acetate [$Ni(Ac)_2{\cdot}4H_2O$, AR], ethylene glycol (EG, AR), and glucose ($C_6H_{12}O_6$, AR) were purchased from Sinopharm Chemical Reagent Co. Ltd. $Mo(CO)_6$ (98%) and $W(CO)_6$ (99%) were purchased from Strem Chemicals Inc. All the chemicals were used as received without further purification. The water (18 megohms/cm) used in all experiments was made by passing through an ultrapure purification system.

Synthesis of subnanometer Pt, PtNi, PtCo, and PtNiCo NWs

In a typical synthesis of Pt NWs, $Pt(acac)_2$ (10.0 mg), $Ni(acac)_2$ (6.4 mg), and $Mo(CO)_6$ (3.0 mg) were dissolved in 5 ml of OA, followed by ultrasonication for 1 hour. The mixture was then heated in an oil bath at 160°C for 2 hours. The cooled product was collected by centrifugation and washed three times with a cyclohexane/ethanol (1:9, v/v) mixture. The preparation of PtNi NWs was similar to that of Pt NWs except for the use of glucose (60 mg) as a reducing agent. The synthesis of PtCo or PtNiCo NWs was similar to that of PtNi NWs except that $Ni(acac)_2$ was replaced with $Co(acac)_3$ (8.9 mg) or the combination of $Ni(acac)_2$ (2.2 mg) and $Co(acac)_3$ (8.9 mg), respectively.

Synthesis of Pt NWs (4.5 nm)

In a typical synthesis of Pt NWs, $Pt(acac)_2$ (20.0 mg), EG (0.1 ml), and ODA (2 g) were added into a glass pressure vessel, followed by magnetic stirring at 80°C for 4 hours under N_2 gas. The mixture was then heated with CO gas at 160°C for 1 hour. The cooled product was collected by centrifugation and washed three times with an ethanol/cyclohexane mixture.

Characterization

TEM and STEM were conducted on an FEI Tecnai F20 transmission electron microscope at an accelerating voltage of 200 kV. SEM images were taken with a Zeiss SEM. The samples were prepared by dropping cyclohexane dispersion of samples onto carbon-coated copper TEM grids using pipettes and dried under ambient condition. XRD patterns were collected on a Shimadzu XRD-6000 x-ray diffractometer. The concentration of catalysts was determined by the ICP-AES (710-ES, Varian, ICP-AES). XPS was conducted on a Thermo Scientific ESCALAB 250 XI x-ray photoelectron spectrometer.

Electrochemical measurements

A three-electrode cell was used to perform the electrochemical measurements. A saturated calomel electrode and a platinum wire were used as the reference electrode and counter electrode, respectively. The catalyst ink was prepared by ultrasonically mixing 2.5 mg of catalysts with 1.78 ml of isopropyl alcohol, 200 μl of water, and 20 μl of 5 weight % (wt %) Nafion solution for 1 hour. Five microliters of the suspension was deposited on a glassy carbon electrode and dried naturally under ambient condition. The loading amount of metal Pt for the Pt NWs (1 nm)/C, Pt NWs (4.5 nm)/C, PtNi NWs/C, and PtNiCo NWs/C catalysts was 6.4 $\mu g/cm^2$. The ECSA was determined by integrating the hydrogen adsorption charge on the CVs at room temperature in N_2-saturated 0.1 M $HClO_4$ solution. Before CV measurements, 30 cycles of potential sweeps were applied. The potential scan rate was 50 mV/s for the CV measurements. ORR measurements were conducted in a 0.1 M $HClO_4$ solution saturated with O_2. The scan and rotation rates for ORR measurement were 10 mV/s and 1600 rpm, respectively. The accelerated durability tests were performed at room temperature in O_2-saturated 0.1 M $HClO_4$ solutions by applying the cyclic potential sweeps between 0.6 and 1.1 V versus RHE at a sweep rate of 100 mV/s for 30,000 cycles. For comparison, the commercial Pt/C (JM, 20 wt % Pt) was used as the benchmark catalyst with the loading amount of 6.4 $\mu g/cm^2$.

DFT models and calculations

For DFT calculations of Pt-based NWs, we used the periodic boundary condition in the x direction, which is along the NW axis, and the NWs were enclosed with 15 Å of vacuum in the other two directions. The E_O value was determined by placing an O atom on an examined adsorption site with the definition $E_O = E[NW + O] - E[NW] - E[O_2]/2$, where $E[NW + O]$ and $E[NW]$ are the total energies of the Pt-based NWs with and without the O adsorbate, respectively. $E[O_2]$ is the total energy of an oxygen molecule. For DFT calculations of total energies, all atoms were fully relaxed.

The DFT calculations were carried out using the Vienna Ab initio Simulation Package (*45*, *46*) with the projector-augmented wave pseudopotentials (*47*) and Perdew-Burke-Ernzerhof generalized gradient approximation (*48*). An energy cutoff of 400 eV was used for the plane-wave basis set. The Brillouin zone was sampled on the basis of the Monkhorst-Pack scheme (*49*) with a 5 × 1 × 1 k-point mesh. The force convergence criterion for atomic relaxation was 0.02 eV/Å.

SUPPLEMENTARY MATERIALS

Supplementary material for this article is available at http://advances.sciencemag.org/cgi/content/full/3/2/e1601705/DC1

fig. S1. TEM, HAADF-STEM images, and histograms of diameter and length of Pt NWs.
fig. S2. XPS spectra of Pt NWs.
fig. S3. Additional HRTEM images of Pt NWs.
fig. S4. TEM, HAADF-STEM images, and histograms of diameter and length of PtNi NWs.
fig. S5. Additional TEM and HRTEM images of PtNi NWs.
fig. S6. STEM image and EDS line scan of PtNi NWs.
fig. S7. TEM images, histograms of diameter and length, PXRD pattern, and EDS pattern of PtCo NWs.
fig. S8. TEM images, histograms of diameter and length, PXRD pattern, and EDS pattern of PtNiCo NWs.
fig. S9. STEM image and EDS line scan of PtNiCo NWs.
fig. S10. TEM images, histograms of diameter and length, PXRD pattern, and EDS pattern of 9-nm Pt NWs and 35-nm Pt NWs.
fig. S11. TEM images of diameter and length changes of Pt NW intermediates obtained with different reaction times.
fig. S12. TEM images of the products collected from the reaction with the same condition used in the synthesis of unique Pt NWs but changing $Mo(CO)_6$.
fig. S13. TEM images of the products collected from the reaction with the same condition used in the synthesis of unique Pt NWs but changing $Ni(acac)_2$.
fig. S14. TEM images of the products collected from the reaction with the same condition used in the synthesis of unique Pt NWs but changing $Ni(acac)_2$ with $Fe(acac)_2$.
fig. S15. TEM images of the products collected from the reaction with the same condition used in the synthesis of unique Pt NWs but with different amount of CTAC.
fig. S16. Fourier transform infrared spectroscopy spectrum of PtNi NWs/C.
fig. S17. TEM images of Pt NWs on commercial carbon.
fig. S18. TEM images of PtNi NWs on commercial carbon.
fig. S19. TEM images of PtNiCo NWs on commercial carbon.
fig. S20. TEM image and diameter histogram of Pt NWs with the diameter of 4.5 nm.
fig. S21. ORR polarization curves, CVs, mass, and specific activities of Pt NWs with different lengths.
fig. S22. TEM images of commercial Pt/C.
fig. S23. CVs of Pt/C, PtNi NWs/C, and PtNiCo NWs/C before and after 30,000 cycles.
fig. S24. TEM image, EDS pattern, and EDS line scan of PtNi NWs/C after 30,000 cycles.
fig. S25. TEM image, EDS pattern, and EDS line scan of PtNiCo NWs/C after 30,000 cycles.
fig. S26. TEM images of commercial Pt/C catalyst after 30,000 cycles.
fig. S27. TEM, PXRD pattern, and EDS pattern of $Pt_{84.4}Ni_{15.6}$ NWs.
fig. S28. TEM, PXRD pattern, and EDS pattern of $Pt_{64.6}Ni_{35.4}$ NWs.
fig. S29. TEM, PXRD pattern, and EDS pattern of $Pt_{78.5}Co_{21.5}$ NWs.
fig. S30. TEM, PXRD pattern, and EDS pattern of $Pt_{67.1}Ni_{23.0}Co_{9.9}$ NWs.
fig. S31. Image of ~50-ml PtNi NW colloidal solution and TEM images of PtNi NWs.
table S1. Atomic ratios of PtNi NWs and PtNiCo NWs characterized by ICP, EDS, and XPS.
table S2. Performance comparisons of various Pt-based NWs and this work.
References (*50*–*55*)

REFERENCES AND NOTES

1. N. Tian, Z.-Y. Zhou, S.-G. Sun, Y. Ding, Z. L. Wang, Synthesis of tetrahexahedral platinum nanocrystals with high-index facets and high electro-oxidation activity. *Science* **316**, 732–735 (2007).
2. V. R. Stamenkovic, B. Fowler, B. S. Mun, G. Wang, P. N. Ross, C. A. Lucas, N. M. Marković, Improved oxygen reduction activity on $Pt_3Ni(111)$ via increased surface site availability. *Science* **315**, 493–497 (2007).
3. G. Chen, C. Xu, X. Huang, J. Ye, L. Gu, G. Li, Z. Tang, B. Wu, H. Yang, Z. Zhao, Z. Zhou, G. Fu, N. Zheng, Interfacial electronic effects control the reaction selectivity of platinum catalysts. *Nat. Mater.* **15**, 564–569 (2016).
4. C. Koenigsmann, S. S. Wong, One-dimensional noble metal electrocatalysts: A promising structural paradigm for direct methanol fuel cells. *Energy Environ. Sci.* **4**, 1161–1176 (2011).
5. B. H. Hong, S. C. Bae, C.-W. Lee, S. Jeong, K. S. Kim, Ultrathin single-crystalline silver nanowire arrays formed in an ambient solution phase. *Science* **294**, 348–351 (2001).
6. B. Wu, A. Heidelberg, J. J. Boland, Mechanical properties of ultrahigh-strength gold nanowires. *Nat. Mater.* **4**, 525–529 (2005).
7. S. Lal, J. H. Hafner, N. J. Halas, S. Link, P. Nordlander, Noble metal nanowires: From plasmon waveguides to passive and active devices. *Acc. Chem. Res.* **45**, 1887–1895 (2012).
8. L. Bu, S. Guo, X. Zhang, X. Shen, D. Su, G. Lu, X. Zhu, J. Yao, J. Guo, X. Huang, Surface engineering of hierarchical platinum-cobalt nanowires for efficient electrocatalysis. *Nat. Commun.* **7**, 11850 (2016).
9. M. P. Zach, K. H. Ng, R. M. Penner, Molybdenum nanowires by electrodeposition. *Science* **290**, 2120–2123 (2000).
10. H. Yin, S. Zhao, K. Zhao, A. Muqsit, H. Tang, L. Chang, H. Zhao, Y. Gao, Z. Tang, Ultrathin platinum nanowires grown on single-layered nickel hydroxide with high hydrogen evolution activity. *Nat. Commun.* **6**, 6430 (2015).
11. M. Reches, E. Gazit, Casting metal nanowires within discrete self-assembled peptide nanotubes. *Science* **300**, 625–627 (2003).
12. F. Patolsky, Y. Weizmann, I. Willner, Actin-based metallic nanowires as bio-nanotransporters. *Nat. Mater.* **3**, 692–695 (2004).
13. L. Mohaddes-Ardabili, H. Zheng, S. B. Ogale, B. Hannoyer, W. Tian, J. Wang, S. E. Lofland, S. R. Shinde, T. Zhao, Y. Jia, L. Salamanca-Riba, D. G. Schlom, M. Wuttig, R. Ramesh, Self-assembled single-crystal ferromagnetic iron nanowires formed by decomposition. *Nat. Mater.* **3**, 533–538 (2004).
14. D. S. Hopkins, D. Pekker, P. M. Goldbart, A. Bezryadin, Quantum interference device made by DNA templating of superconducting nanowires. *Science* **308**, 1762–1765 (2005).

15. X. Guo, Y. Ying, L. Tong, Photonic nanowires: From subwavelength waveguides to optical sensors. *Acc. Chem. Res.* **47**, 656–666 (2013).
16. J. F. Fennell Jr., S. F. Liu, J. M. Azzarelli, J. G. Weis, S. Rochat, K. A. Mirica, J. B. Ravnsbæk, T. M. Swager, Nanowire chemical/biological sensors: Status and a roadmap for the future. *Angew. Chem. Int. Ed.* **55**, 1266–1281 (2016).
17. F. Favier, E. C. Walter, M. P. Zach, T. Benter, R. M. Penner, Hydrogen sensors and switches from electrodeposited palladium mesowire arrays. *Science* **293**, 2227–2231 (2001).
18. M. Shao, A. Peles, K. Shoemaker, Electrocatalysis on platinum nanoparticles: Particle size effect on oxygen reduction reaction activity. *Nano Lett.* **11**, 3714–3719 (2011).
19. E. Antolini, Structural parameters of supported fuel cell catalysts: The effect of particle size, inter-particle distance and metal loading on catalytic activity and fuel cell performance. *Appl. Catal. B Environ.* **181**, 298–313 (2016).
20. F. J. Perez-Alonso, D. N. McCarthy, A. Nierhoff, P. Hernandez-Fernandez, C. Strebel, I. E. L. Stephens, J. H. Nielsen, I. Chorkendorff, The effect of size on the oxygen electroreduction activity of mass-selected platinum nanoparticles. *Angew. Chem. Int. Ed.* **51**, 4641–4643 (2012).
21. F. Calle-Vallejo, J. Tymoczko, V. Colic, Q. H. Vu, M. D. Pohl, K. Morgenstern, D. Loffreda, P. Sautet, W. Schuhmann, A. S. Bandarenka, Finding optimal surface sites on heterogeneous catalysts by counting nearest neighbors. *Science* **350**, 185–189 (2015).
22. M. Nesselberger, S. Ashton, J. C. Meier, I. Katsounaros, K. J. J. Mayrhofer, M. Arenz, The particle size effect on the oxygen reduction reaction activity of Pt catalysts: Influence of electrolyte and relation to single crystal models. *J. Am. Chem. Soc.* **133**, 17428–17433 (2011).
23. Y. Sun, L. Zhuang, J. Lu, X. Hong, P. Liu, Collapse in crystalline structure and decline in catalytic activity of Pt nanoparticles on reducing particle size to 1 nm. *J. Am. Chem. Soc.* **129**, 15465–15467 (2007).
24. Y. Xia, P. Yang, Y. Sun, Y. Wu, B. Mayers, B. Gates, Y. Yin, F. Kim, H. Yan, One-dimensional nanostructures: Synthesis, characterization, and applications. *Adv. Mater.* **15**, 353–389 (2003).
25. H.-l. Liu, F. Nosheen, X. Wang, Noble metal alloy complex nanostructures: Controllable synthesis and their electrochemical property. *Chem. Soc. Rev.* **44**, 3056–3078 (2015).
26. T. Ling, J.-J. Wang, H. Zhang, S.-T. Song, Y.-Z. Zhou, J. Zhao, X.-W. Du, Freestanding ultrathin metallic nanosheets: Materials, synthesis, and applications. *Adv. Mater.* **27**, 5396–5402 (2015).
27. B. Y. Xia, H. B. Wu, Y. Yan, X. W. Lou, X. Wang, Ultrathin and ultralong single-crystal platinum nanowire assemblies with highly stable electrocatalytic activity. *J. Am. Chem. Soc.* **135**, 9480–9485 (2013).
28. C. Wang, Y. Hou, J. Kim, S. Sun, A general strategy for synthesizing FePt nanowires and nanorods. *Angew. Chem. Int. Ed.* **46**, 6333–6335 (2007).
29. H. Duan, N. Yan, R. Yu, C.-R. Chang, G. Zhou, H.-S. Hu, H. Rong, Z. Niu, J. Mao, H. Asakura, T. Tanaka, P. J. Dyson, J. Li, Y. Li, Ultrathin rhodium nanosheets. *Nat. Commun.* **5**, 3093 (2014).
30. X. Huang, S. Tang, X. Mu, Y. Dai, G. Chen, Z. Zhou, F. Ruan, Z. Yang, N. Zheng, Freestanding palladium nanosheets with plasmonic and catalytic properties. *Nat. Nanotechnol.* **6**, 28–32 (2011).
31. Y. N. Xia, Y. J. Xiong, B. Lim, S. E. Skrabalak, Shape-controlled synthesis of metal nanocrystals: Simple chemistry meets complex physics? *Angew. Chem. Int. Ed.* **48**, 60–103 (2009).
32. W. Zhou, J. Wu, H. Yang, Highly uniform platinum icosahedra made by hot injection-assisted GRAILS method. *Nano Lett.* **13**, 2870–2874 (2013).
33. S. Guo, D. Li, H. Zhu, S. Zhang, N. M. Markovic, V. R. Stamenkovic, S. Sun, FePt and CoPt nanowires as efficient catalysts for the oxygen reduction reaction. *Angew. Chem. Int. Ed.* **52**, 3465–3468 (2013).
34. L. Ma, C. Wang, B. Y. Xia, K. Mao, J. He, X. Wu, Y. Xiong, X. W. Lou, Platinum multicubes prepared by Ni^{2+}-mediated shape evolution exhibit high electrocatalytic activity for oxygen reduction. *Angew. Chem. Int. Ed.* **54**, 5666–5671 (2015).
35. J. Chen, T. Herricks, M. Geissler, Y. Xia, Single-crystal nanowires of platinum can be synthesized by controlling the reaction rate of a polyol process. *J. Am. Chem. Soc.* **126**, 10854–10855 (2004).
36. L. Bu, J. Ding, S. Guo, X. Zhang, D. Su, X. Zhu, J. Yao, J. Guo, G. Lu, X. Huang, A general method for multimetallic platinum alloy nanowires as highly active and stable oxygen reduction catalysts. *Adv. Mater.* **27**, 7204–7212 (2015).
37. N. T. Khi, J. Yoon, H. Kim, S. Lee, B. Kim, H. Baik, S. J. Kwon, K. Lee, Axially twinned nanodumbbell with a Pt bar and two Rh@Pt balls designed for high catalytic activity. *Nanoscale* **5**, 5738–5742 (2013).
38. X. Huang, Z. Zhao, Y. Chen, E. Zhu, M. Li, X. Duan, Y. Huang, A rational design of carbon-supported dispersive Pt-based octahedra as efficient oxygen reduction reaction catalysts. *Energy Environ. Sci.* **7**, 2957–2962 (2014).
39. R. M. Arán-Ais, F. Dionigi, T. Merzdorf, M. Gocyla, M. Heggen, R. E. Dunin-Borkowski, M. Gliech, J. Solla-Gullón, E. Herrero, J. M. Feliu, Elemental anisotropic growth and atomic-scale structure of shape-controlled octahedral Pt–Ni–Co alloy nanocatalysts. *Nano Lett.* **15**, 7473–7480 (2015).
40. B. Han, C. E. Carlton, J. Suntivich, Z. Xu, Y. Shao-Horn, Oxygen reduction activity and stability trends of bimetallic $Pt_{0.5}M_{0.5}$ nanoparticle in acid. *J. Phys. Chem. C* **119**, 3971–3978 (2015).
41. H.-H. Li, S.-Y. Ma, Q.-Q. Fu, X.-J. Liu, L. Wu, S.-H. Yu, Scalable bromide-triggered synthesis of Pd@Pt core–shell ultrathin nanowires with enhanced electrocatalytic performance toward oxygen reduction reaction. *J. Am. Chem. Soc.* **137**, 7862–7868 (2015).
42. S. Guo, S. Zhang, D. Su, S. Sun, Seed-mediated synthesis of core/shell FePtM/FePt (M = Pd, Au) nanowires and their electrocatalysis for oxygen reduction reaction. *J. Am. Chem. Soc.* **135**, 13879–13884 (2013).
43. V. Stamenkovic, B. S. Mun, K. J. Mayrhofer, P. N. Ross, N. M. Markovic, J. Rossmeisl, J. Greeley, J. K. Nørskov, Changing the activity of electrocatalysts for oxygen reduction by tuning the surface electronic structure. *Angew. Chem. Int. Ed.* **118**, 2963–2967 (2006).
44. J. K. Nørskov, J. Rossmeisl, A. Logadottir, L. Lindqvist, J. R. Kitchin, T. Bligaard, H. Jónsson, Origin of the overpotential for oxygen reduction at a fuel-cell cathode. *J. Phys. Chem. B* **108**, 17886–17892 (2004).
45. G. Kresse, J. Hafner, Ab initio molecular dynamics for liquid metals. *Phys. Rev. B* **47**, 558 (1993).
46. G. Kresse, J. Furthmüller, Efficient iterative schemes for *ab initio* total-energy calculations using a plane-wave basis set. *Phys. Rev. B* **54**, 11169 (1996).
47. P. E. Blöchl, Projector augmented-wave method. *Phys. Rev. B* **50**, 17953 (1994).
48. J. P. Perdew, K. Burke, M. Ernzerhof, Generalized gradient approximation made simple. *Phys. Rev. Lett.* **77**, 3865–3868 (1996).
49. H. J. Monkhorst, J. D. Pack, Special points for Brillouin-zone integrations. *Phys. Rev. B* **13**, 5188 (1976).
50. M. A. Hoque, F. M. Hassan, D. Higgins, J.-Y. Choi, M. Pritzker, S. Knights, S. Ye, Z. Chen, Multigrain platinum nanowires consisting of oriented nanoparticles anchored on sulfur-doped graphene as a highly active and durable oxygen reduction electrocatalyst. *Adv. Mater.* **27**, 1229–1234 (2015).
51. L. Ruan, E. Zhu, Y. Chen, Z. Lin, X. Huang, X. Duan, Y. Huang, Biomimetic synthesis of an ultrathin platinum nanowire network with a high twin density for enhanced electrocatalytic activity and durability. *Angew. Chem. Int. Ed.* **52**, 12577–12581 (2013).
52. S. Sun, G. Zhang, D. Geng, Y. Chen, R. Li, M. Cai, X. Sun, A highly durable platinum nanocatalyst for proton exchange membrane fuel cells: Multiarmed starlike nanowire single crystal. *Angew. Chem. Int. Ed.* **123**, 442–446 (2011).
53. B. Y. Xia, W. T. Ng, H. B. Wu, X. Wang, X. W. D. Lou, Self-supported interconnected Pt nanoassemblies as highly stable electrocatalysts for low-temperature fuel cells. *Angew. Chem. Int. Ed.* **124**, 7325–7328 (2012).
54. C. Koenigsmann, A. C. Santulli, K. Gong, M. B. Vukmirovic, W.-p. Zhou, E. Sutter, S. S. Wong, R. R. Adzic, Enhanced electrocatalytic performance of processed, ultrathin, supported Pd–Pt core–shell nanowire catalysts for the oxygen reduction reaction. *J. Am. Chem. Soc.* **133**, 9783–9795 (2011).
55. H. Zhu, S. Zhang, S. Guo, D. Su, S. Sun, Synthetic control of FePtM nanorods (M = Cu, Ni) to enhance the oxygen reduction reaction. *J. Am. Chem. Soc.* **135**, 7130–7133 (2013).

Acknowledgments

Funding: This work was financially supported by the Ministry of Science and Technology (2016YFA0204100), National Basic Research Program of China (2016YFB0100201), National Natural Science Foundation of China (21571135 and 51671003), Young Thousand Talented Program, the start-up funding from Soochow University and Peking University, and the Priority Academic Program Development of Jiangsu Higher Education Institutions. Work at California State University, Northridge, was supported by the Army Research Office via grant W911NF-11-1-0353. **Author contributions:** X.H. and S.G. conceived and supervised the research. X.H. and K.J. designed the experiments. X.H., K.J., D.Z., S.G., X. Zhang, X. Zhu, J.G., and G.L. performed most of the experiments and data analysis. X.H., K.J., D.Z., S.G., X. Zhang, X. Zhu, J.G., and G.L. participated in various aspects of the experiments and discussions. X.Z. and G.L. performed the DFT simulations. X.H., S.G., and K.J. wrote the paper. All authors discussed the results and commented on the manuscript. **Competing interests:** The authors declare that they have no competing interests. **Data and materials availability:** All data needed to evaluate the conclusions in the paper are present in the paper and/or the Supplementary Materials. Additional data related to this paper may be requested from the authors.

Submitted 25 July 2016
Accepted 28 December 2016
Published 24 February 2017
10.1126/sciadv.1601705

Citation: K. Jiang, D. Zhao, S. Guo, X. Zhang, X. Zhu, J. Guo, G. Lu, X. Huang, Efficient oxygen reduction catalysis by subnanometer Pt alloy nanowires. *Sci. Adv.* **3**, e1601705 (2017).